CHAPTER VII
NON-ISOTHERMAL MELT-CRYSTALLIZATION AND MECHANICAL PROPERTIES OF TITANIUM(IV)OXIDE NANOPARTICLE-FILLED ISOTACTIC POLYPROPYLENE

7.1 Abstract

The present contribution reports an investigation on the effect of the addition of titanium(IV)oxide (TiO_2) with diverse surface characteristics [i.e. neat, silica (SiO_2)-coated and stearic acid-coated] and various contents (ranging from 5 to 30 wt%) on non-isothermal melt-crystallization, subsequent melting behavior and mechanical properties of filled isotactic polypropylene (iPP). The cooling rate used ranged between 5 and 30°C min^{-1}. The crystallization exotherm for all of the samples investigated became larger and shifted towards a lower temperature as the cooling rate increased. The crystallization peak temperature (T_p) values for all of the iPP samples filled with neat TiO_2 nanoparticles were slightly greater than those of the neat iPP and were not affected by the variation in the filler content. For iPP samples filled with stearic acid-coated TiO_2 nanoparticles, the T_p values were not much different from those of the neat iPP. For iPP samples filled with 5, 20, and 30wt% SiO_2-coated TiO_2 nanoparticles, marked differences in the T_p values in comparison with those of the neat iPP were observed. Together with the Avrami analysis, the nucleation ability of the various fillers investigated can be ranked as follows: SiO_2-coated TiO_2 nanoparticles > neat TiO_2 nanoparticles > stearic acid-coated TiO_2 nanoparticles. Lastly, the presence of the nanoparticles caused the rigidity of the resulting composites to increase (especially when the filler content was greater than or equal to 20 wt%.

7.2 Introduction

Inorganic fillers have always played an important role in the plastics and rubber industries. The main purpose of their use is confined not only to cost reduction, but also to improve physical and mechanical performance such as color, rigidity, dimensional stability, toughness and transparency [1,2]. The level of such an improvement depends significantly on type, size and shape, content, and surface treatment of the fillers [3–6]. The latter influences directly the interaction between the polymer matrix and the fillers at the interface. Among the various mineral fillers, calcium carbonate ($CaCO_3$) and titanium dioxide (TiO_2) have been among the most utilized materials. While the use of $CaCO_3$ has been due to its low cost [6,7], TiO_2 is mainly used as a white pigment, due to its brightness. In addition, TiO_2 can act as a flame retardant or antioxidant that could help improve the thermal stability of the final products [8–10].

Inorganic nanoparticles are interesting as a new class of inorganic fillers because of the high specific surface area. Both the isothermal and non-isothermal crystallization studies of silica (SiO_2) nanoparticle-filled isotactic polypropylene (iPP) nanocomposites have been carried out by a number of research groups [11–13]. Qian et al. [11] reported that the non-isothermal melt-crystallization behavior of iPP samples filled with SiO_2 nanoparticles exhibited much lower induction periods and greater crystallization rates in comparison with those of the neat ones. Papageorgiou et al. [12] studied the crystallization kinetics of iPP samples filled with SiO_2 nanoparticles and found that the crystallization rates of the nanocomposites were faster than the neat iPP, due to the existence of the SiO_2 nanoparticles that could reduce the critical nucleus size needed for crystal growth or reduce the work needed to create a new surface. Jain et al. [13] reported the preparation of iPP/SiO_2 nanoparticle composites via the sol–gel method and found that nucleation efficiency of such composites was much greater than that of the similar composites previously reported.

In the present contribution, the non-isothermal melt-crystallization of isotactic polypropylene (iPP) filled with neat, SiO_2-coated and stearic acid-coated

TiO_2 nanoparticles was investigated mainly by differential scanning calorimetry (DSC). The kinetics of the non-isothermal melt-crystallization process was analyzed based on the Avrami macrokinetic model. The mechanical properties (i.e. tensile strength, impact strength, and flexural strength) were also evaluated and reported.

7.3 Theoretical Background

In DSC, the energy released during a non-isothermal crystallization process appears to be a function of temperature. As a result, the relative crystallinity as a function of temperature $\theta(T)$ can be formulated as

$$\theta(T) = \frac{\int_{T_0}^{T} (\mathrm{d}H_c/\mathrm{d}T')\mathrm{d}T'}{\Delta H_c}, \tag{7.1}$$

where T_0 and T represent the onset and an arbitrary temperature, respectively, $\mathrm{d}H_c$ is the enthalpy of crystallization released during an infinitesimal temperature range $\mathrm{d}T$, and ΔH_c is the total enthalpy of crystallization for a specific cooling condition.

To use Eq. (7.1) in analyzing the non-isothermal crystallization data obtained by DSC, it is assumed that the sample experiences a similar thermal condition as designated by the DSC furnace. This can only be realized when the difference between the temperatures of the sample and the furnace is minimal. If this condition is valid, the relation between the crystallization time t and the sample temperature T can be written as

$$t = \frac{T_0 - T}{\phi}, \tag{7.2}$$

where T_0 is an arbitrary initial temperature and ϕ is the cooling rate. According to Eq. (7.2), the horizontal temperature axis observed in a DSC thermogram for the non-isothermal crystallization data can then be transformed into the time domain.

Among the various macrokinetic models, the Avrami proposition [14–16] is the most common equation used to describe the overall isothermal crystallization kinetics. In this model, the relative crystallinity as a function of time $\theta(t)$ can be expressed as

$$\theta(t) = 1 - \exp\left[-(K_A t)^{n_A}\right], \tag{7.3}$$

where K_A and n_A are the Avrami rate constant and the Avrami exponent, respectively. Both K_A and n_A are constants specific to a given crystalline morphology and type of nucleation for a particular crystallization condition [17] and the units of K_A are given as an inverse of time. Although the Avrami equation is often used to describe the isothermal crystallization behavior of semi-crystalline polymers, it has also been applied to describe the non-isothermal crystallization behavior of semi-crystalline polymers [18,19].

7.4 Experimental

7.4.1 Materials

The commercial general purpose grade of iPP (HP 400K) used in this study was supplied by HMC Polymers Co., Ltd. (Rayong, Thailand). Certain properties of the resin, provided by the manufacturer, are as follows: MFR (2.16 kg at 190°C) = 4g· (10 min)$^{-1}$, density = 0.9 g cm^{-3}, tensile strength at yield = 33MPa, elongation at yield = 10%, flexural modulus = 1400MPa and notched Izod impact strength at 23°C = 30 J m^{-1}. TiO_2 nanoparticles with different surface characteristics (i.e. neat, SiO_2-coated, and stearic acid-coated) were supplied by Advanced

Nanotechnology Co., Ltd. (Samutprakarn, Thailand). Some specific properties of the three grades are summarized in Table 7.1. Hereafter, CYU201, CYU202, and CYU203 were used to denote the neat, the SiO_2-coated and the stearic acid-coated TiO_2 nanoparticles, respectively.

Table 7.1 Specific properties of the TiO_2 nanoparticles

Property	CYU 201	CYU 202	CYU 203
Average particle size (nm)	50	50	50
Crystal type	Rutile	Rutile	Rutile
Content of TiO_2 (%)	98	95	92
Specific surface area (m^2/g)	>35	>35	>35
Surface properties	Hydrophilic	Hydrophilic	Hydrophobic
Surface treatment agent	no	SiO_2	Fatty acid

7.4.2 Sample Preparation

Each type of TiO_2 nanoparticles was first dried in an oven at 80°C for 24h and then pre-mixed with iPP pellets in a tumble mixer for 20 min to achieve dry blends in various contents of TiO_2 nanoparticles (i.e. 5, 10, 20, and 30 wt%). The as-prepared dry blends were then fed into a Collin ZK25 self-wiping, co-rotating twin screw extruder operating at a screw speed of 80 rpm and a temperature profile of 185°C (die zone), 190°C (zone 5), 185°C (zone 4), 180°C (zone 3), 175°C (zone 2), and 100°C (feed zone). The extrudate was cooled in a water bath and later cut into pellets by a Planetrol 075D2 pelletizer.

Each of the as-prepared compounds was dried inan oven at 60°C overnight, prior to being shaped into film and mechanical test specimens. A part of each sample was then compressed into thin films between a pair of transparency films set between a pair of stainless steel platens in a Wabash V50H compression press, at 190°C. After 2 min holding at 190°C, the film moldings were allowed to cool at ambient condition between the transparency films and the stainless steel platens. Another part of the sample was injection-molded into mechanical test specimens according to the ISO 527-1 (for tensile test specimens), ISO 180 (for

impact test specimens), and ISO 178 standard test methods, using an ARBURG Allrounder® 270M injection molding machine. The temperature settings (from the feed zone to the nozzle) were 150, 160, 170, 180, and 190°C, respectively. The injection pressure was 1000 bar and the dwelling pressure was 700 bar. Prior to the mechanical tests, all of the test specimens were conditioned under ambient condition for 7 days.

7.4.3 Differential Scanning Calorimetry Measurements

The non-isothermal melt-crystallization and subsequent melting behavior of neat iPP and iPP samples filled with TiO_2 nanoparticles with different surface characteristics were measured by a Mettler-Toledo DSC822^e differential scanning calorimeter (DSC). The calibration was carried out with an indium standard (T_m^0 = 156.6°C and ΔH_f^0 = 28.5 J g^{-1}) on every other run to ensure accuracy and reliability of the obtained data. To minimize thermal lag between the polymer sample and the DSC furnace, each sample holder was loaded with a disc-shaped sample (4.2±0.8 mg) cut from the as-prepared films (0.18±0.03mm thick). Each sample was used only once and all the runs were carried out under nitrogen atmosphere (flow rate = 60 ml min^{-1}).

The measurements started with heating each sample from 25 to 190°C at a heating rate of 80°C min^{-1}. This treatment was to set a similar thermal history to all of the samples investigated. To ensure complete melting, each sample was melt-annealed at 190°C for 5 min, after which time the sample was cooled at a desired cooling rate (ϕ), ranging from 5 to 30°C min^{-1}, to 25°C. The subsequent melting behavior was then observed by reheating the sample at a heating rate of 10°C min^{-1} to 190°C. Both non-isothermal melt-crystallization exotherms and subsequent melting endotherms were recorded for further analysis.

7.4.4 Mechanical Testing

Tensile strength at yield, elongation at yield, and Young's modulus for both neat iPP and iPP samples filled with TiO_2 nanoparticles with different surface characteristics were measured on an Instron 4206 universal testing machine, according to the ISO 527-1 standard test method, using a 100 kN load cell, a 50 mm min^{-1} crosshead

speed and a 50 mm gauge length. The Izod impact resistance for all of the samples was determined on a Zwick 5113 impact tester according to a similar procedure to that described in the ISO 180 standard test method, with the original size of each specimen being about $27 \times 62 \times 4$ mm^3 using a 2.7 J pendulum and a 124.4° release angle. Flexural strength and flexural modulus for all of the samples were determined on test specimens cut from the molded dumbbells according to the procedure described in the ISO 178 standard test method using the three-point loading fixture of the Instron 4206 universal testing machine. All of the mechanical measurements were carried out at room temperature (26±1°C) and the results were reported as averages of the data taken from at least 10 specimens.

7.5 Results and Discussion

7.5.1 Non-Isothermal Melt-Crystallization and Subsequent Melting Behavior

Fig. 7.1 shows non-isothermal melt-crystallization exotherms of neat iPP at six different cooling rates, ranging from 5 to 30°C min^{-1}. As expected, the crystallization exotherm became larger and shifted to a lower temperature with increasing cooling rate. This observation is attributed to the kinetic effect which is normally found for crystallization in a nucleation-controlled region. At a low cooling rate, there was sufficient time for athermal nuclei with large enough size to become stable at a high temperature, thus the crystallization could begin at a high temperature. At a greater cooling rate, the polymer molecules experienced much faster decrease in the temperature, thus athermal nuclei with much smaller size could become stable, leading to the observed decrease in temperature range where the polymer started crystallizing. Though not shown, iPP samples filled with TiO_2 nanoparticles behaved in a similar manner, with an exception for the ones filled with 30 wt% CYU202 which exhibited a double crystallization behavior (see later).

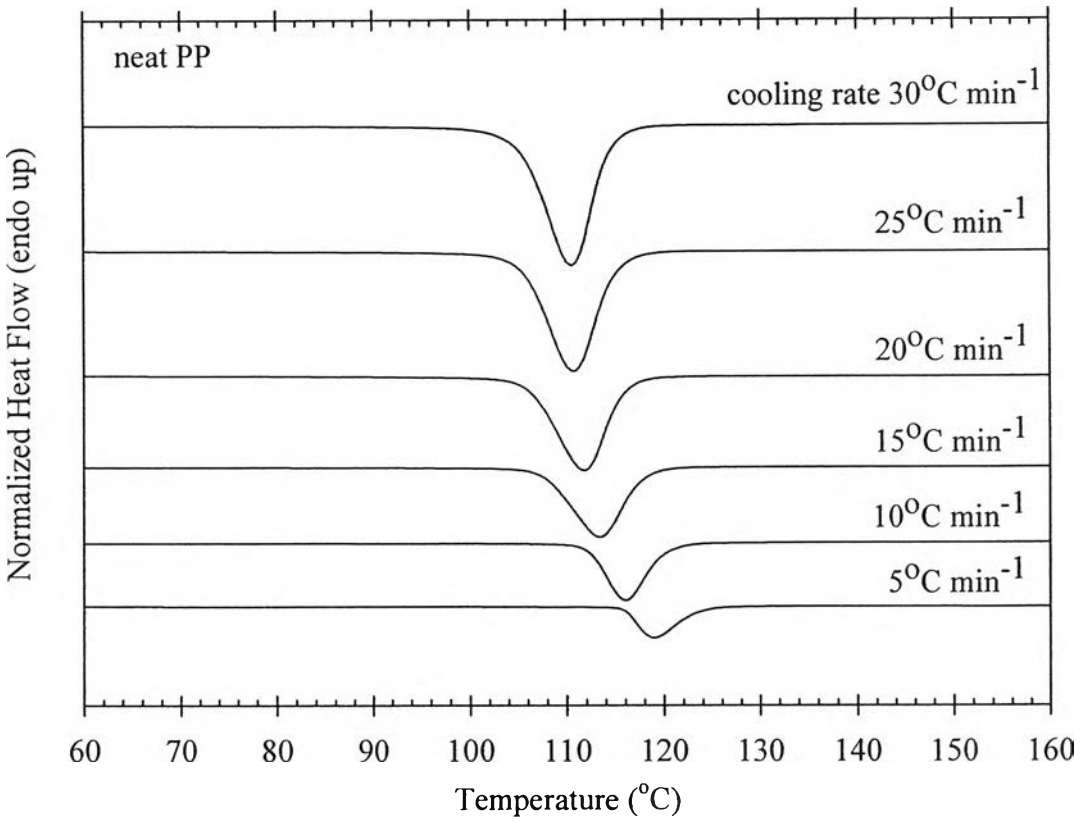

Figure 7.1 Non-isothermal melt-crystallization exotherm of neat iPP at six different cooling rates.

Based on these exotherms, some quantitative data [i.e. the temperature at 1% relative crystallinity ($T_{0.01}$), the temperature at the maximum crystallization rate or the crystallization peak temperature (T_p), and the temperature at 99% relative crystallinity ($T_{0.99}$)] can be obtained and the results are summarized in Table 7.2. However, for iPP samples filled with 30 wt% CYU202, due to the presence of the double crystallization peaks, only the peak temperatures of the low and the high crystallization exotherms (T_{cl} and T_{ch}, respectively) are listed. Obviously, these values ($T_{0.01}$, T_p, and $T_{0.99}$) shifted towards lower temperature values with increasing cooling rate. It should be noted that $T_{0.01}$ and $T_{0.99}$ represent the onset and the ending points of the non-isothermal melt-crystallization process in the temperature domain.

Table 7.2 Characteristic data of non-isothermal melt-crystallization exotherms for neat and TiO_2-filled iPP

ϕ ($^{o}C\ min^{-1}$)	$T_{0.01}$ (^{o}C)	T_p (^{o}C)	$T_{0.99}$ (^{o}C)	$T_{0.01}$ (^{o}C)	T_p (^{o}C)	$T_{0.99}$ (^{o}C)
	Neat iPP					
5	123.6	119.0	115.9			
10	120.1	116.0	112.1			
15	117.9	113.3	107.5			
20	116.1	111.9	106.0			
25	115.3	110.5	105.2			
30	114.8	110.5	104.8			
	iPP + 5wt% CYU201			iPP + 10wt% CYU201		
5	123.3	120.4	117.5	123.8	120.7	117.6
10	121.0	117.9	114.1	121.0	117.8	113.5
15	119.4	116.0	111.2	119.2	115.8	111.6
20	118.1	114.5	109.8	117.7	113.9	108.9
25	117.5	114.1	108.5	117.5	114.0	108.1
30	116.7	112.8	106.5	116.4	112.5	106.6
	iPP + 20wt% CYU201			iPP + 30wt% CYU201		
5	124.5	120.8	117.6	125.5	121.7	118.6
10	121.4	118.3	114.6	121.6	118.2	114.8
15	119.7	116.4	112.1	120.0	116.1	111.9
20	118.3	114.5	109.6	118.1	114.8	110.5
25	117.3	113.7	108.3	117.0	113.3	108.7
30	116.3	112.7	106.4	116.5	112.6	106.9

Table 7.2 Characteristic data of non-isothermal melt-crystallization exotherms for neat and TiO_2-filled iPP (*continued*)

ϕ (°C min^{-1})	$T_{0.01}$ (°C)	T_p (°C)	$T_{0.99}$ (°C)	$T_{0.01}$ (°C)	T_p (°C)	$T_{0.99}$ (°C)
	iPP + 5wt% CYU202			iPP + 10wt% CYU202		
5	124.8	122.8	120.8	123.7	120.2	117.3
10	123.2	121.2	118.5	120.8	116.9	113.5
15	121.7	120.2	116.9	119.1	115.1	111.0
20	120.9	119.1	114.6	117.4	113.5	108.9
25	120.5	118.8	113.9	116.5	112.7	107.8
30	119.8	117.8	112.4	115.5	111.3	106.1
	iPP + 20wt% CYU202			iPP + 30wt% CYU202		
				T_{cl}	T_{ch}	
5	129.1	126.5	123.7	-	127.5	
10	126.6	123.6	119.4	118.6	123.4	
15	125.0	121.8	117.8	116.3	120.9	
20	122.8	119.4	115.1	114.7	120.3	
25	121.8	118.5	113.3	113.0	119.3	
30	121.7	118.6	112.8	112.1	117.3	
	iPP + 5wt% CYU203			iPP + 10wt% CYU203		
5	123.5	118.6	114.9	125.0	120.3	116.3
10	120.6	115.0	111.4	121.4	116.2	111.4
15	117.8	112.7	108.6	119.2	113.9	109.2
20	116.6	111.5	106.6	117.4	112.4	107.3
25	115.7	110.3	103.7	116.5	111.4	105.6
30	113.8	108.0	101.5	115.5	110.0	103.8
	iPP + 20wt% CYU203			iPP + 30wt% CYU203		
5	124.9	120.5	117.2	124.8	120.6	117.4
10	122.4	117.6	113.7	120.2	116.4	112.6
15	120.0	115.2	110.9	118.5	113.7	108.4
20	118.9	113.8	108.6	116.9	113.3	108.8
25	117.4	112.2	106.6	116.0	111.8	106.6
30	115.7	111.0	104.7	115.2	111.1	104.2

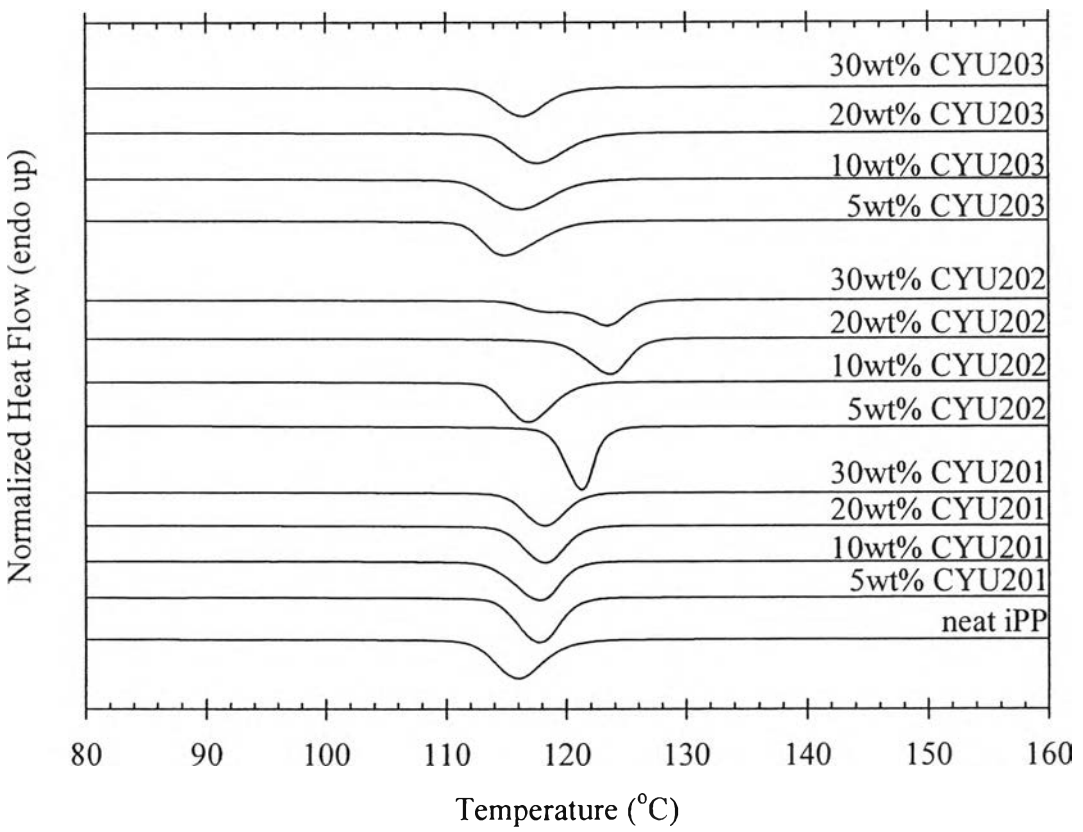

Figure 7.2 Non-isothermal melt-crystallization exotherm of neat and TiO_2-filled iPP recorded at a cooling rate of 10°C min^{-1}.

Fig. 7.2 shows non-isothermal melt-crystallization exotherms of neat iPP and iPP samples filled with TiO_2 nanoparticles having different surface characteristics at different loadings for a fixed cooling rate of 10°C min^{-1}. Even though only the results for the cooling rate of 10°C min^{-1} are shown, the discussion of the results was carried out based on the results summarized in Table 7.2. Apparently, the T_p values for all of the iPP samples filled with CYU201 were slightly greater than those of the neat iPP (by about 1.4–3.6°C) and were not affected by the variation in the CYU201 content (about 2.3–2.6°C on average for different CYU201 contents). For iPP samples filled with CYU203, the T_p values for all of the iPP

samples filled with 5 wt% CYU203 were slightly lower than those of the neat iPP (by about 0.2–2.5 1C). With increasing CYU203 content from 5 to 20 wt%, the T_p values were found to increase from those of the neat iPP samples and then decrease as its content increased to 30 wt%.

For iPP samples filled with CYU202, the difference between the T_p values for all of the filled iPP samples and those of the neat iPP ones was the greatest among the various TiO_2 nanoparticles investigated (with the exception of the iPP samples filled with 10 wt% CYU202 which exhibited slightly greater T_p values than those of the neat iPP samples). Specifically, such a difference in the T_p values was about 6.5°C for the samples filled with 5 wt% and about 7.9°C for the samples filled with 20 and 30 wt% on average. Based on the results obtained, the ability of both the neat and the stearic acid-coated TiO_2 nanoparticles in nucleating iPP was inferior to that of the SiO_2-coated ones. A number of research groups reported that SiO_2 particles are a good nucleating agent for iPP [11–13]. Previously, it has been reported that the ability of TiO_2 particles in nucleating syndiotactic polypropylene (sPP) was also inferior to that of SiO_2 particles [20] and that surface coating of $CaCO_3$ particles with stearic acid and paraffin reduced the nucleating ability of the particles [6].

As clearly observed in Fig. 7.2, the exotherm for the iPP sample filled with 30 wt% CYU202 exhibited double crystallization peaks. To clearly illustrate the occurrence of the double crystallization behavior for this particular composite, the non-isothermal melt-crystallization exotherms for the iPP samples filled with 30 wt% CYU202 recorded at six different cooling rates are shown in Fig. 7.3. For these, only the peak temperatures of the low and the high crystallization exotherms (T_{cl} and T_{ch}, respectively) are reported in Table 7.2. Clearly, all of the exotherms exhibited double crystallization peaks, except that recorded at 5°C min^{-1} exhibiting only one peak. Repeated experiments confirmed that such an observation was not an artifact. Previously, Supaphol et al. [6] observed double crystallization peaks for sPP samples filled with a high content of 1.9 mm uncoated $CaCO_3$ particles and attributed the phenomenon to the self-nucleation of sPP on sPP crystallites entrapped within the rough surface of the filler. Double crystallization was also reported for iPP samples filled with 25 vol.% of 1.3 mm uncoated $CaCO_3$ particles by Pukánszky and Fekete [21].

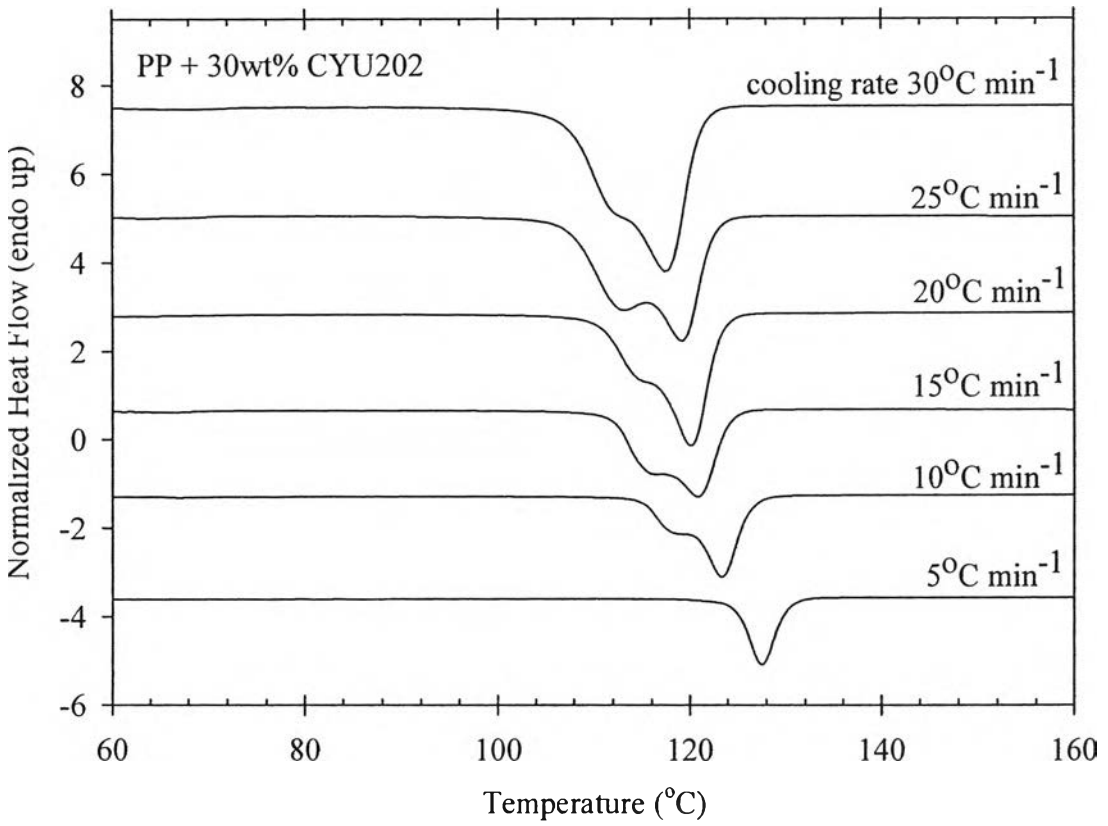

Figure 7.3 Non-isothermal melt-crystallization exotherms of iPP filled with 30wt% CYU202 at six different cooling rates.

Another possible explanation for the occurrence of the double crystallization behavior of iPP samples filled with 30 wt% CYU202 is the existence of two effective nucleation sites on the surface of the nanoparticles. For CYU202 grade, the surface of TiO_2 nanoparticles is coated with SiO_2. If the coverage of SiO_2 on the surface of the particles was not perfect, there could be partial area where the surface of pure TiO_2 was exposed. If one compares the T_{cl} values of iPP samples filled with 30 wt% CYU202 against the T_p values of iPP samples filled with CYU201 at the same filler content (see Table 7.2), one can notice that the listed values are comparable to each other (at any given cooling rate). This confirms the occurrence of the low crystallization exotherm being a result of the crystallization of

iPP on the exposed TiO_2 sites on the particles. If the occurrence of the low crystallization exotherm is indeed due to the nucleation of iPP on the exposed TiO_2 sites on the particles, it can be further assumed that the occurrence of the high crystallization exotherm is a result of the nucleation of iPP on the SiO_2 sites on the particles. Despite the occurrence of the double crystallization peaks, the melting thermograms of these samples exhibited only one melting endotherm (results not shown), indicating the formation of one crystalline phase despite the suggestion of possible multiple nucleation sites with different efficiencies.

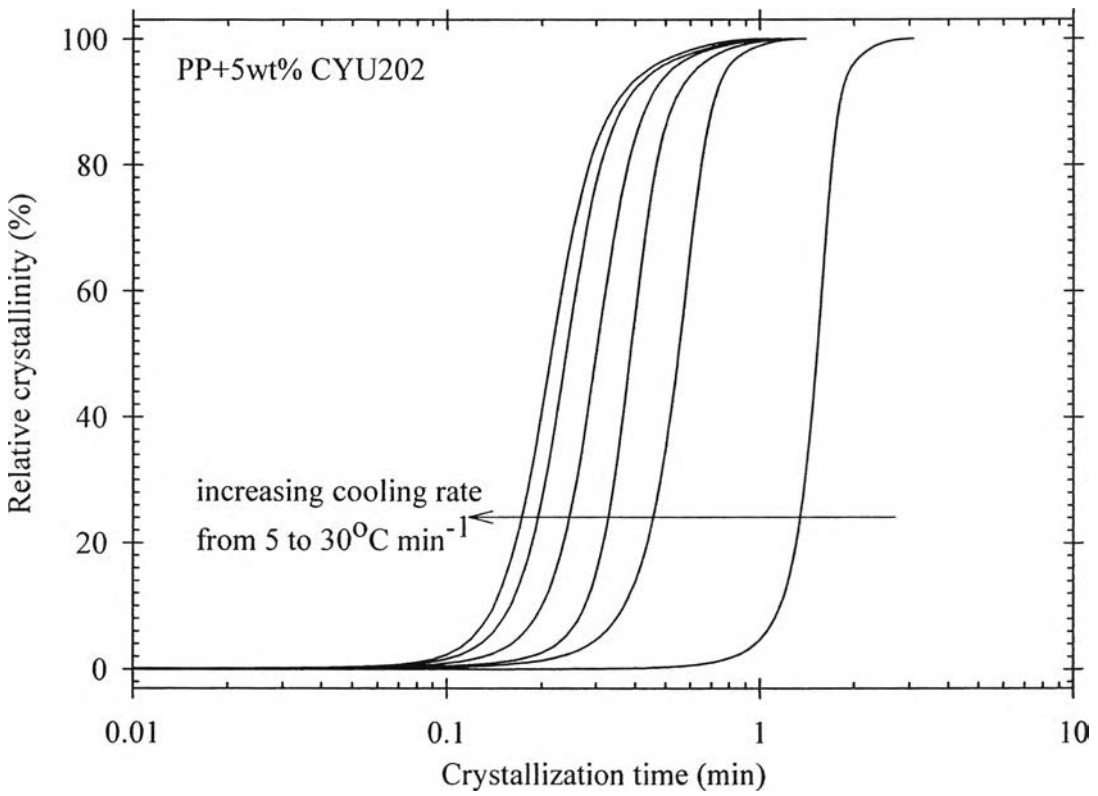

Figure 7.4 Relative crystallinity as a function of time for iPP filled with 5wt% CYU202 at six different cooling rates after excluding an induction period.

The data such as those shown in Fig. 7.1 can be further analyzed by converting the non-isothermal melt-crystallization exotherm to the relative crystallinity as a function of time $\theta(t)$ using Eq. (7.1) along with Eq. (7.2). The converted curves for iPP samples filled with 5wt% CYU202 at six different cooling rates are illustrated in Fig. 7.4. Clearly, the faster the cooling rate, the shorter the time required for the completion of the crystallization process. Other samples including those of neat iPP exhibited a similar behavior. These $\theta(t)$ curves did not include the apparent incubation period Δt_{inc}, defined as a time period during which the polymer is still in the molten state [i.e. $\Delta t_{inc} = (T_f - T_{onset})/\phi$, where T_f is the temperature at which a polymer sample was brought to melt, T_{onset} is the actual temperature where the sample began to crystallize, and ϕ is the cooling rate]. The Δt_{inc} values were calculated based on a fixed T_f value of 190°C and the results are summarized in Tables 7.3–7.6 for neat iPP and iPP samples filled with CYU201, CYU202, and CYU203, respectively. For each sample, Δt_{inc} decreased monotonically with increasing cooling rate.

Table 7.3 Quantitative analysis of the relative crystallinity as a functions of time for neat iPP

ϕ (°C min^{-1})	Δt_{inc} (min)	t_θ (min)							Δt_c (min)
		θ= 0.01	θ= 0.1	θ= 0.3	θ= 0.5	θ= 0.7	θ= 0.9	θ= 0.99	
	Neat iPP								
5	12.44	0.44	1.07	1.46	1.70	1.90	2.15	2.65	2.22
10	6.49	0.27	0.61	0.81	0.93	1.03	1.18	1.48	1.21
15	4.50	0.18	0.41	0.56	0.65	0.74	0.88	1.14	0.96
20	3.45	0.15	0.32	0.42	0.49	0.56	0.66	0.92	0.77
25	2.79	0.12	0.26	0.35	0.41	0.46	0.55	0.80	0.68
30	2.33	0.11	0.24	0.31	0.35	0.40	0.48	0.72	0.61

Table 7.4 Quantitative analysis of the relative crystallinity as a functions of time for iPP filled with CYU201

ϕ (°C min^{-1})	Δt_{inc} (min)	t_θ (min)							Δt_c (min)
		θ= 0.01	θ= 0.1	θ= 0.3	θ= 0.5	θ= 0.7	θ= 0.9	θ= 0.99	
	iPP + 5wt% CYU201								
5	12.64	0.41	0.88	1.14	1.31	1.47	1.70	2.32	1.91
10	6.59	0.19	0.43	0.58	0.68	0.77	0.90	1.23	1.04
15	4.50	0.15	0.31	0.41	0.49	0.56	0.68	0.93	0.78
20	3.43	0.11	0.24	0.33	0.38	0.44	0.53	0.82	0.71
25	2.76	0.10	0.21	0.28	0.33	0.38	0.46	0.73	0.63
30	2.34	0.08	0.17	0.23	0.28	0.32	0.41	0.63	0.55
	iPP + 10wt% CYU201								
5	12.55	0.40	0.88	1.16	1.34	1.50	1.73	2.25	1.86
10	6.59	0.20	0.45	0.60	0.70	0.80	0.96	1.33	1.12
15	4.49	0.15	0.32	0.43	0.50	0.57	0.68	1.02	0.86
20	3.44	0.13	0.26	0.35	0.41	0.47	0.57	0.87	0.74
25	2.77	0.10	0.21	0.28	0.33	0.38	0.47	0.75	0.65
30	2.34	0.09	0.18	0.24	0.29	0.33	0.41	0.67	0.58
	iPP + 20wt% CYU201								
5	12.29	0.41	1.00	1.35	1.55	1.73	1.99	2.52	2.11
10	6.60	0.16	0.38	0.52	0.61	0.70	0.83	1.13	0.97
15	4.49	0.13	0.29	0.40	0.47	0.54	0.64	0.89	0.77
20	3.43	0.10	0.23	0.31	0.37	0.43	0.52	0.79	0.69
25	2.78	0.08	0.20	0.27	0.32	0.36	0.45	0.67	0.58
30	2.36	0.07	0.17	0.23	0.27	0.32	0.39	0.55	0.48
	iPP + 30wt% CYU201								
5	12.30	0.35	0.83	1.15	1.34	1.52	1.77	2.34	1.98
10	6.50	0.21	0.45	0.61	0.70	0.79	0.92	1.29	1.08
15	4.38	0.17	0.37	0.49	0.57	0.64	0.75	1.01	0.84
20	3.41	0.12	0.26	0.34	0.39	0.44	0.53	0.83	0.71
25	2.78	0.10	0.21	0.27	0.32	0.36	0.45	0.69	0.59
30	2.32	0.09	0.18	0.25	0.29	0.33	0.41	0.62	0.53

Table 7.5 Quantitative analysis of the relative crystallinity as a functions of time for iPP filled with CYU202

ϕ (^{o}C min^{-1})	Δt_{inc} (min)	t_θ (min)							Δt_c (min)
		$\theta=$ 0.01	$\theta=$ 0.1	$\theta=$ 0.3	$\theta=$ 0.5	$\theta=$ 0.7	$\theta=$ 0.9	$\theta=$ 0.99	
	iPP + 5wt% CYU202								
5	12.25	0.39	0.86	1.09	1.22	1.33	1.50	2.07	1.68
10	6.40	0.17	0.35	0.46	0.53	0.59	0.69	1.10	0.93
15	4.33	0.13	0.26	0.33	0.38	0.42	0.52	0.86	0.73
20	3.31	0.11	0.20	0.26	0.30	0.35	0.44	0.78	0.67
25	2.66	0.09	0.17	0.22	0.25	0.29	0.38	0.72	0.63
30	2.24	0.09	0.15	0.19	0.22	0.26	0.36	0.69	0.60
	iPP + 10wt% CYU202								
5	12.59	0.38	0.86	1.16	1.35	1.51	1.74	2.22	1.85
10	6.53	0.22	0.50	0.67	0.78	0.87	1.01	1.33	1.10
15	4.52	0.15	0.31	0.42	0.50	0.56	0.66	0.90	0.75
20	3.44	0.12	0.26	0.36	0.42	0.47	0.56	0.79	0.67
25	2.79	0.11	0.22	0.29	0.33	0.38	0.46	0.69	0.59
30	2.35	0.10	0.20	0.26	0.30	0.34	0.42	0.63	0.53
	iPP + 20wt% CYU202								
5	11.58	0.34	0.76	1.02	1.17	1.33	1.64	2.41	2.07
10	6.06	0.18	0.40	0.54	0.64	0.74	0.94	1.45	1.27
15	4.14	0.12	0.28	0.37	0.44	0.51	0.63	1.02	0.90
20	3.22	0.09	0.21	0.28	0.34	0.39	0.49	0.85	0.76
25	2.61	0.08	0.19	0.25	0.30	0.35	0.45	0.79	0.71
30	2.16	0.08	0.17	0.23	0.27	0.31	0.40	0.72	0.64

Table 7.6 Quantitative analysis of the relative crystallinity as a functions of time for iPP filled with CYU203

ϕ (°C min^{-1})	Δt_{inc} (min)	t_θ (min)							Δt_c (min)
		θ= 0.01	θ= 0.1	θ= 0.3	θ= 0.5	θ= 0.7	θ= 0.9	θ= 0.99	
	iPP + 5wt% CYU203								
5	12.50	0.49	1.10	1.49	1.74	1.97	2.26	3.02	2.54
10	6.56	0.25	0.56	0.78	0.92	1.03	1.18	1.62	1.37
15	4.50	0.17	0.41	0.56	0.65	0.73	0.84	1.10	0.92
20	3.43	0.14	0.31	0.43	0.50	0.57	0.66	0.91	0.76
25	2.77	0.12	0.28	0.38	0.44	0.51	0.62	0.82	0.70
30	2.33	0.11	0.27	0.35	0.41	0.46	0.56	0.77	0.66
	iPP + 10wt% CYU203								
5	12.14	0.49	1.14	1.54	1.78	2.01	2.32	3.04	2.56
10	6.37	0.30	0.66	0.88	1.02	1.16	1.34	1.78	1.48
15	4.36	0.22	0.47	0.63	0.72	0.81	0.93	1.29	1.08
20	3.34	0.18	0.38	0.49	0.57	0.63	0.74	1.13	0.95
25	2.65	0.16	0.35	0.45	0.52	0.58	0.68	1.02	0.86
30	2.23	0.14	0.31	0.40	0.45	0.50	0.60	0.94	0.80
	iPP + 20wt% CYU203								
5	12.08	0.48	1.14	1.53	1.77	1.97	2.23	2.95	2.48
10	6.23	0.30	0.66	0.88	1.01	1.12	1.28	1.78	1.47
15	4.29	0.22	0.47	0.62	0.71	0.79	0.91	1.31	1.09
20	3.25	0.18	0.38	0.50	0.58	0.65	0.75	1.08	0.90
25	2.65	0.16	0.33	0.42	0.49	0.54	0.64	0.95	0.79
30	2.24	0.15	0.29	0.37	0.42	0.47	0.57	0.90	0.75
	iPP + 30wt% CYU203								
5	12.13	0.46	1.10	1.49	1.71	1.91	2.16	2.76	2.30
10	6.44	0.30	0.64	0.83	0.94	1.04	1.20	1.76	1.46
15	4.42	0.20	0.45	0.60	0.69	0.78	0.92	1.25	1.04
20	3.41	0.16	0.33	0.42	0.48	0.54	0.63	0.96	0.80
25	2.73	0.14	0.29	0.37	0.42	0.48	0.57	0.84	0.69
30	2.31	0.12	0.25	0.32	0.37	0.42	0.52	0.76	0.64

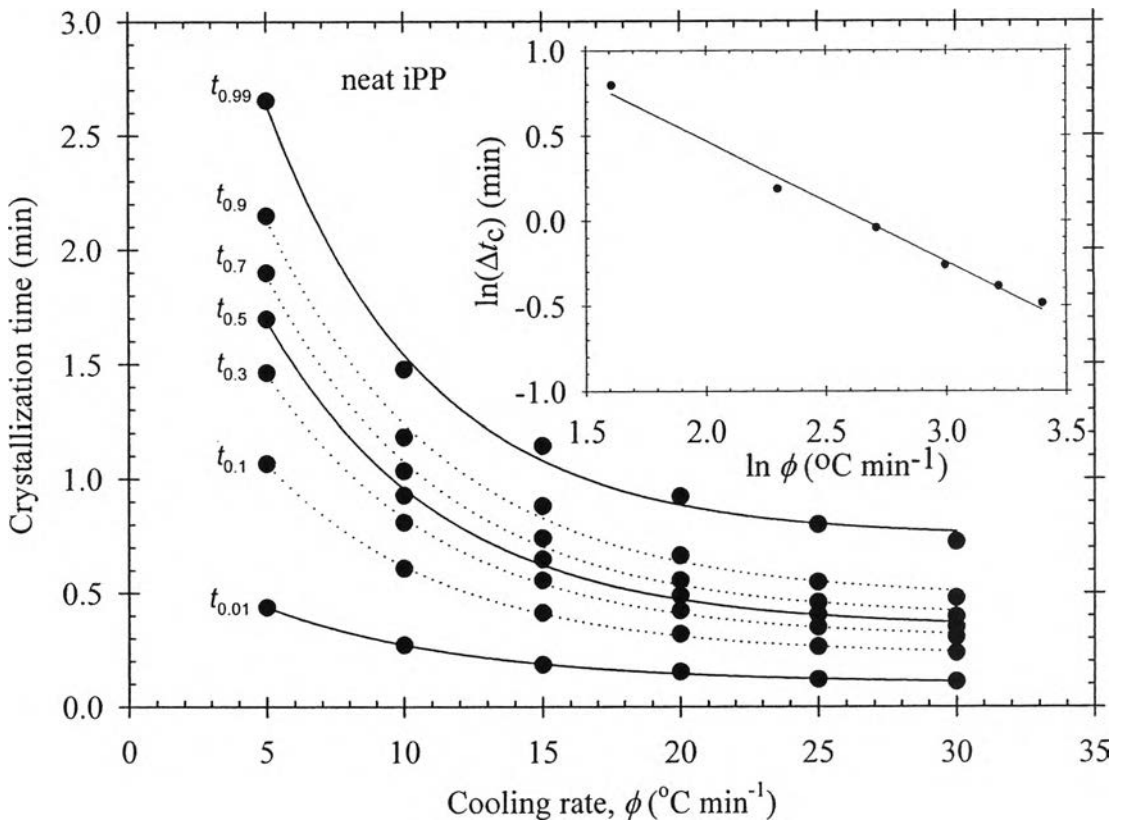

Figure 7.5 Crystallization time at various relative crystallinity values as a function of cooling rate for neat iPP. The inset figure shows a relationship between apparent total crystallization period and cooling rate in a log-log plot.

Furthermore, the crystallization time at an arbitrary relative crystallinity ty can be determined from the $\theta(t)$ curves. The t_θ values after exclusion of the respective Δt_{inc} values for various relative crystallinities (i.e. θ = 0.01, 0.1, 0.3, 0.5, 0.7, 0.9, and 0.99) for all of the samples investigated are also summarized in Tables 7.3–7.6, while Fig. 7.5 shows plots of t_θ as a function of cooling rate for neat iPP. The apparent total crystallization period Δt_c can be calculated directly from the difference between the apparent ending and the apparent onset of the crystallization

process in the time domain (i.e. $\Delta t_c = t_{0.99} - t_{0.01}$). These values for all of the samples investigated are also summarized in Tables 7.3–7.6. According to the data presented in these tables, the t_θ for a given value of θ and the Δt_c decreased withincreasing cooling rate. In an attempt to further analyze the results shown in these tables, plots of $\ln(\Delta t_c)$ versus $\ln(\phi)$ (shown as an inset in Fig. 7.5 for neat iPP) and of $\ln(t_\theta)$ versus $\ln(\phi)$ (shown in Fig. 7.6 for neat iPP) were carried out. Interestingly, the linearity of these plots is evident. Table 7.7 summarizes values of the y-intercept and the slope obtained from these plots for all of the samples investigated. Interestingly, the *y*-intercept of these plots was found to increase with increasing y value, while the slope was not found to exhibit a specific trend.

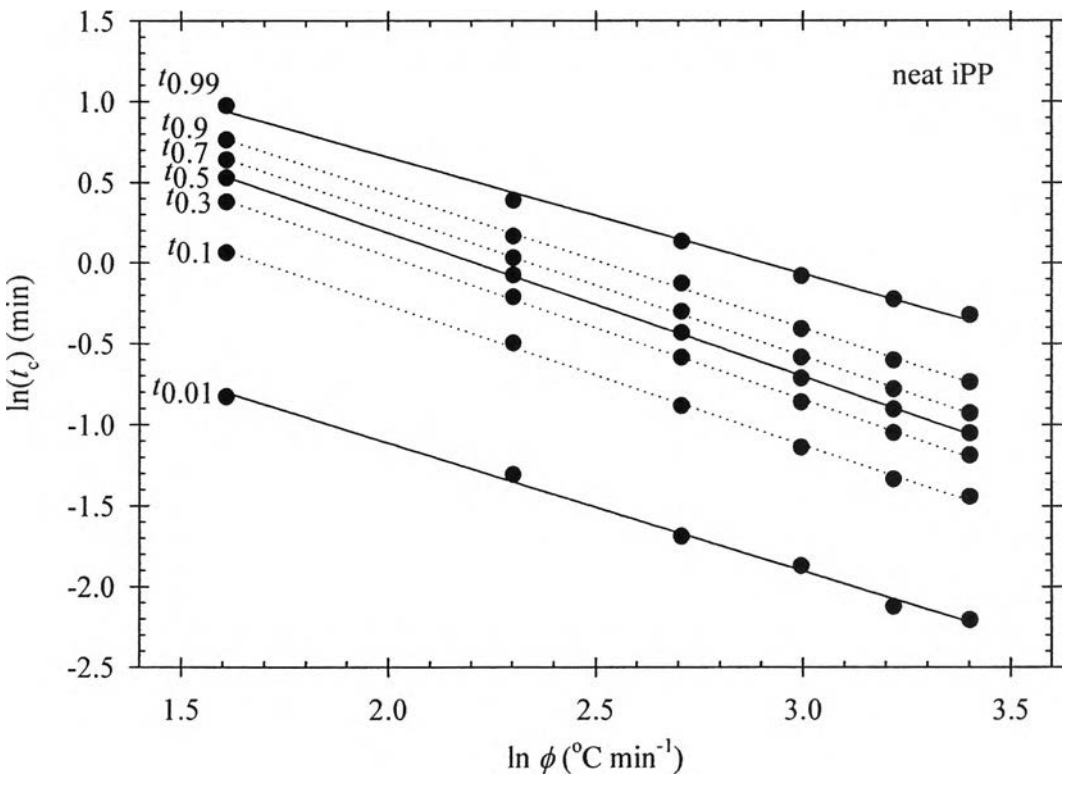

Figure 7.6 Crystallization time at various relative crystallinity values as a function of cooling rate in a log-log plot for neat iPP.

Table 7.7 y-intercept, slope, and the r^2 values of regression lines drawn through plots of $\ln(t_\theta)$ versus $\ln(\phi)$ for various θ values

θ	y-intercept (min)	slope ($min^2\ ^oC^{-1}$)	r^2	y-intercept (min)	slope ($min^2\ ^oC^{-1}$)	r^2
	Neat iPP					
0.01	0.47	-0.790	0.9956			
0.1	1.46	-0.860	0.9985			
0.3	1.81	-0.886	0.9994			
0.5	1.96	-0.889	0.9997			
0.7	2.06	-0.880	0.9996			
0.9	2.12	-0.841	0.9990			
0.99	2.10	-0.724	0.9955			
Δt_c	1.89	-0.711	0.9917			
	iPP + 5wt% CYU201			iPP + 10wt% CYU201		
0.01	0.44	-0.869	0.9911	0.40	-0.840	0.9955
0.1	1.27	-0.893	0.9963	1.25	-0.874	0.9977
0.3	1.51	-0.874	0.9977	1.51	-0.864	0.9979
0.5	1.62	-0.857	0.9980	1.64	-0.853	0.9981
0.7	1.71	-0.839	0.9979	1.73	-0.838	0.9982
0.9	1.78	-0.796	0.9962	1.81	-0.798	0.9975
0.99	1.90	-0.702	0.9828	1.86	-0.670	0.9965
Δt_c	1.66	-0.672	0.9796	1.62	-0.640	0.9963
	iPP + 20wt% CYU201			iPP + 30wt% CYU201		
0.01	0.46	-0.922	0.9685	0.22	-0.775	0.9938
0.1	1.42	-0.961	0.9728	1.19	-0.847	0.9909
0.3	1.72	-0.954	0.9753	1.53	-0.865	0.9905
0.5	1.84	-0.941	0.9767	1.69	-0.866	0.9908
0.7	1.92	-0.922	0.9775	1.79	-0.859	0.9910
0.9	2.00	-0.881	0.9751	1.88	-0.823	0.9918
0.99	2.11	-0.797	0.9711	1.99	-0.732	0.9957
Δt_c	1.90	-0.776	0.9712	1.81	-0.724	0.9939

Table 7.7 y-intercept, slope, and the r^2 values of regression lines drawn through plots of $\ln(t_\theta)$ versus $\ln(\phi)$ for various θ values *(continued)*

θ	y-intercept (min)	slope ($min^2\ ^oC^{-1}$)	r^2	y-intercept (min)	slope ($min^2\ ^oC^{-1}$)	r^2
	iPP + 5wt% CYU202			iPP + 10wt% CYU202		
0.01	0.25	-0.819	0.9705	0.24	-0.767	0.9914
0.1	1.29	-0.959	0.9826	1.20	-0.843	0.9912
0.3	1.55	-0.961	0.9867	1.52	-0.854	0.9939
0.5	1.62	-0.939	0.9867	1.67	-0.853	0.9951
0.7	1.64	-0.899	0.9841	1.77	-0.845	0.9960
0.9	1.58	-0.792	0.9704	1.85	-0.811	0.9958
0.99	1.60	-0.607	0.9506	1.92	-0.714	0.9889
Δt_c	1.33	-0.568	0.9462	1.71	-0.703	0.9876
	iPP + 20wt% CYU202					
0.01	0.28	-0.864	0.9908			
0.1	1.07	-0.855	0.9906			
0.3	1.36	-0.854	0.9943			
0.5	1.50	-0.845	0.9953			
0.7	1.61	-0.833	0.9953			
0.9	1.77	-0.808	0.9914			
0.99	1.95	-0.689	0.9883			
Δt_c	1.76	-0.665	0.9875			
	iPP + 5wt% CYU203			iPP + 10wt% CYU203		
0.01	0.58	-0.835	0.9928	0.39	-0.694	0.9983
0.1	1.34	-0.812	0.9853	1.27	-0.730	0.9907
0.3	1.68	-0.823	0.9910	1.63	-0.763	0.9942
0.5	1.84	-0.827	0.9921	1.81	-0.775	0.9953
0.7	1.95	-0.820	0.9906	1.94	-0.781	0.9954
0.9	2.02	-0.787	0.9841	2.05	-0.765	0.9937
0.99	2.31	-0.784	0.9816	2.12	-0.660	0.9860
Δt_c	2.12	-0.775	0.9787	1.93	-0.653	0.9815

Table 7.7 y-intercept, slope, and the r^2 values of regression lines drawn through plots of $\ln(t_\theta)$ versus $\ln(\phi)$ for various θ values *(continued)*

θ	y-intercept (min)	slope ($min^2\ ^oC^{-1}$)	r^2	y-intercept (min)	slope ($min^2\ ^oC^{-1}$)	r^2
	iPP + 20wt% CYU203			iPP + 30wt% CYU203		
0.01	0.33	-0.672	0.9961	0.47	-0.754	0.9957
0.1	1.36	-0.772	0.9990	1.47	-0.844	0.9973
0.3	1.70	-0.795	0.9995	1.80	-0.866	0.9966
0.5	1.85	-0.802	0.9995	1.94	-0.869	0.9955
0.7	1.95	-0.798	0.9994	2.03	-0.860	0.9937
0.9	2.02	-0.767	0.9979	2.09	-0.822	0.9910
0.99	2.15	-0.679	0.9932	2.24	-0.747	0.9957
Δt_c	1.97	-0.681	0.9921	2.05	-0.746	0.9951

Fig. 7.7 shows subsequent melting endotherms of neat iPP after non-isothermally crystallized at six different cooling rates, ranging from 5 to 30°C min^{-1}. These thermograms were recorded at a fixed heating rate of 10°C min^{-1}. Apparently, the double melting behavior was observed for the neat iPP samples crystallized at cooling rates greater than about 10°C min^{-1}. The low melting peak temperature (T_{m3}) shifted towards a lower temperature with increasing cooling rate, while the high melting peak temperature (T_{m4}) increased very slightly. The occurrence of the high-temperature melting endotherm was postulated to be a result of the melting of the recrystallized materials formed during a heating scan [22,23]. On the other hand, the occurrence of the low-temperature melting endotherm should correspond to the melting of the crystallites originally formed during a cooling scan [23]. In addition, the observed decrease in the T_{m3} values with increasing cooling rate implied that the crystallites formed during a fast cooling scan were less stable than those formed during a slower cooling scan.

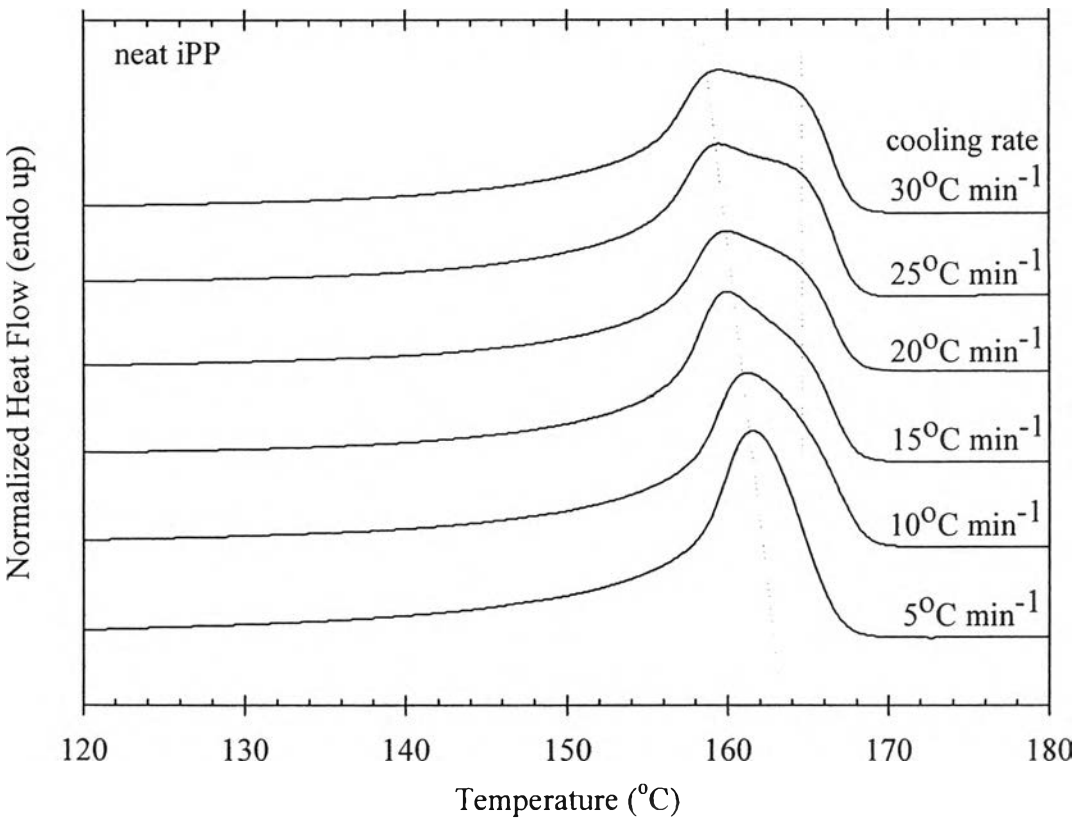

Figure 7.7 Subsequent melting endotherm (recorded at 10°C min^{-1}) of neat iPP after non-isothermal melt-crystallization at six different cooling rates.

Fig. 7.8 shows subsequent melting endotherms of iPP samples filled with 20 wt% CYU203 after non-isothermally crystallized at six different cooling rates, ranging from 5 to 30°C min^{-1}. Evidently, multiple melting endotherms were observed for this particular composite. As many as four endotherms were observed for the sample non-isothermally crystallized at 30°C min^{-1}, while about two endotherms were observed for the sample nonisothermally crystallized at 5°C min^{-1}. The major endothermic peak(s) at temperatures around 160–165°C should correspond to the melting of the crystallites originally formed during a cooling scan and the melting of the recrystallized materials formed during a heating scan, as

previously discussed. The small melting endotherm (T_{m1}) at a temperature around 145°C should correspond to the melting of the crystallites of a different crystalline phase, i.e. the β-phase. Trongtorsak et al. [24] reported the melting of a heterophasic copolymer of isotactic polypropylene and ethylene–propylene rubber (iPP/EPR blend) which was nucleated with a β-nucleator occurring at temperatures around 147–153°C. In addition, the other small melting endotherm (T_{m2}) at a temperature around 155°C should correspond to the melting of α'-crystallites which were formed by the transformation of the less stable β-crystallites during a heating scan [22].

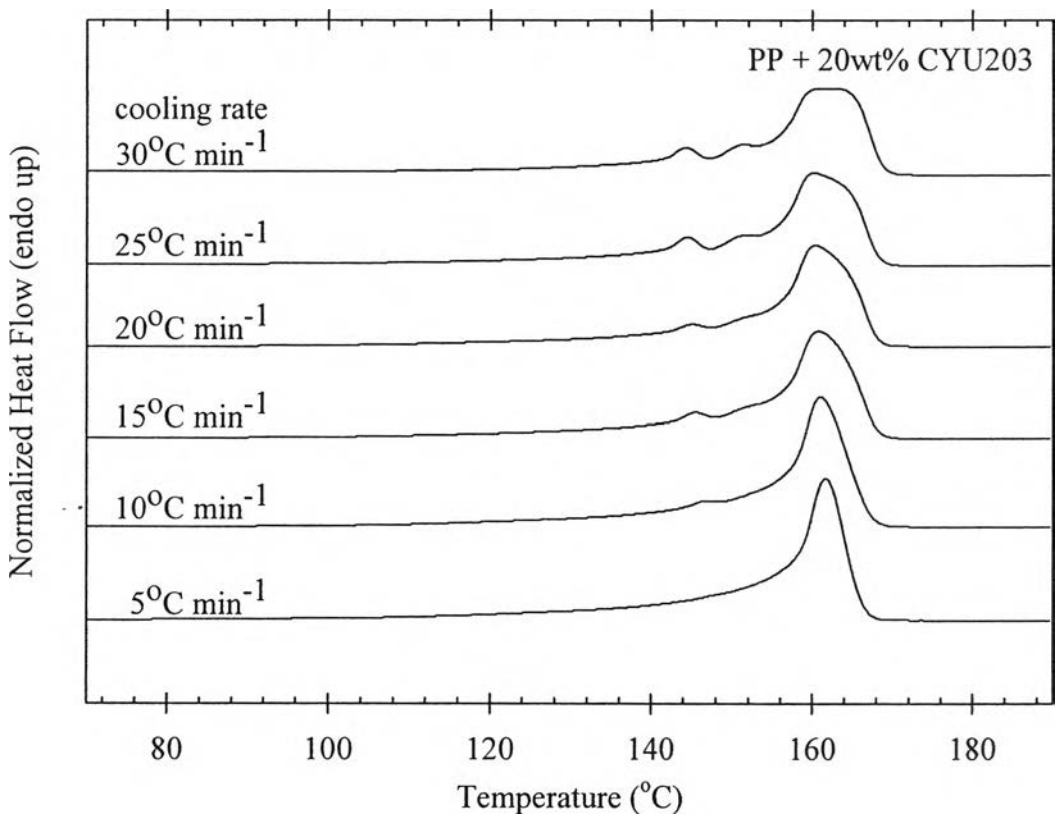

Figure 7.8 Subsequent melting endotherm (recorded at 10°C min^{-1}) of iPP filled with 20wt% CYU203 after non-isothermal melt-crystallization at six different cooling rates.

For all of the samples investigated, the melting peak temperature(s) is/are summarized in Table 7.8.

Table 7.8 Characteristic data of subsequent melting endotherms after non-isothermal melt-crystallization for neat and TiO_2-filled iPP

ϕ (°C min^{-1})	T_{m1} (°C)	T_{m2} (°C)	T_{m3} (°C)	T_{m4} (°C)	T_{m1} (°C)	T_{m2} (°C)	T_{m3} (°C)	T_{m4} (°C)
	Neat iPP							
5	-	-	161.6	-				
10	-	-	160.6	165.7				
15	-	-	159.5	165.4				
20	-	-	159.1	165.4				
25	-	-	158.8	165.5				
30	-	-	158.6	165.3				
	iPP + 5wt% CYU201				iPP + 10wt% CYU201			
5	-	-	160.1	-	-	152.2	161.2	-
10	-	151.2	160.5	-	-	151.6	160.1	162.3
15	-	-	157.8	163.8	-	151.1	157.7	163.4
20	-	151.7	157.2	163.2	-	149.9	158.4	163.4
25	-	149.8	157.0	163.7	-	149.7	158.6	164.7
30	-	150.3	157.9	164.3	-	149.4	157.6	164.2
	iPP + 20wt% CYU201				iPP + 30wt% CYU201			
5	148.4	152.6	161.4	-	-		161.4	-
10	146.8	150.6	160.3	-	-	149.4	160.0	-
15	-	151.7	159.7	-	-	148.6	159.7	-
20	-	149.8	158.8	163.4	-	151.8	159.4	-
25	145.0	151.8	159.2	164.8	-	148.2	159.0	164.5
30	144.8	150.0	159.2	165.0	-	147.3	158.0	164.2

Table 7.8 Characteristic data of subsequent melting endotherms after non-isothermal melt-crystallization for neat and TiO_2-filled iPP (*continued*)

ϕ (°C min^{-1})	T_{m1} (°C)	T_{m2} (°C)	T_{m3} (°C)	T_{m4} (°C)	T_{m1} (°C)	T_{m2} (°C)	T_{m3} (°C)	T_{m4} (°C)
	iPP + 5wt% CYU202				iPP + 10wt% CYU202			
5	-	-	-	162.1	-	152.9	161.8	-
10	-	-	-	161.6	-	151.4	159.4	-
15	-	-	-	161.1	-	150.9	158.7	163.9
20	-	-	-	161.2	-	150.4	156.4	163.4
25	-	-	-	160.8	-	153.2	156.9	162.0
30	-	-	-	160.8	-	150.3	155.5	163.4
	iPP + 20wt% CYU202				iPP + 30wt% CYU202			
5	-	-	-	163.0	-	-	155.3	163.7
10	-	-	-	162.3	-	-	153.9	163.3
15	-	-	-	162.3	-	-	-	161.6
20	-	-	-	161.2	-	-	-	161.3
25	-	-	-	160.6	-	-	-	160.9
30	-	-	-	160.8	-	-	-	161.2
	iPP + 5wt% CYU203				iPP + 10wt% CYU203			
5	-	-	161.4	-	-	-	162.5	-
10	-	-	159.8	165.2	145.8	151.6	160.0	-
15	144.5	150.9	159.1	165.2	145.0	151.1	159.6	164.9
20	144.3	150.8	159.0	165.5	144.3	150.6	159.0	164.9
25	143.8	150.6	159.5	165.6	144.4	150.9	159.5	165.9
30	144.0	150.5	159.1	166.1	144.3	150.8	159.7	165.9
	iPP + 20wt% CYU203				iPP + 30wt% CYU203			
5	-	-	161.6	-	-	-	162.1	-
10	146.5	-	160.6	-	146.4	-	160.4	-
15	145.3	151.6	160.0	-	145.9	-	160.5	-
20	145.0	151.3	159.7	165.4	145.0	151.0	159.6	165.1
25	144.5	151.0	159.3	165.4	144.3	150.8	159.0	165.1
30	144.3	150.8	159.2	165.8	144.3	150.8	159.1	165.4

7.5.2 Non-Isothermal Melt-Crystallization Based on Avrami Analysis

The analysis of the non-isothermal melt-crystallization data based on the Avrami model can be carried out through a plot between ln[-ln(1-$\theta(t)$)] and ln(t), such as those shown in Fig. 7.9 for neat iPP. Due to the non-linearity of the plot, only the data in the relative crystallinity range of 10–80% were used in the analysis. The deviation from the linearity was a result of the secondary crystallization process. Table 7.9 summarizes values of the Avrami kinetic parameters (i.e. K_A and n_A) along with the values of the r^2 parameter signifying the quality of the fitting. Based on the values of r^2, it can be concluded that the Avrami model was suitable for describing the non-isothermal melt-crystallization of these samples. For a given sample type, the Avrami rate constant K_A increased monotonously with increasing cooling rate, indicating that crystallization proceeded much faster as the cooling rate increased. At a given cooling rate, the K_A values of the iPP samples filled with CYU201 and CYU202 were greater, while those of the iPP samples filled with CYU203 were lower, than those of the neat iPP samples. Among the various types of TiO_2 nanoparticles, CYU202 was the best in enhancing the crystallization rates of the iPP matrix. Clearly, neat and stearic acid-coated TiO_2 nanoparticles (CYU201 and CYU203, respectively) were not effective nucleating agents for iPP. On the contrary, SiO_2-coated TiO_2 nanoparticles (CYU202) increased the crystallization rates of the iPP matrix appreciably, an indication of a good nucleating agent for iPP.

With regards to the Avrami exponent n_A, it ranged between 4.6 and 5.7 for neat iPP, between 3.8 and 6.3 for iPP filled with CYU201, between 3.9 and 7.3 for iPP filled with CYU202, and between 4.3 and 6.1 for iPP filled with CYU203, respectively.

Table 7.9 Non-isothermal melt-crystallization kinetics for neat and TiO_2-filled based on Avrami analysis over the crystallinity range of 10 to 80%

ϕ (°C min^{-1})	K_A (min^{-1})	n_A	r^2	K_A (min^{-1})	n_A	r^2
	Neat iPP					
5	0.47	5.21	0.9984			
10	0.86	5.69	0.9992			
15	1.32	4.60	0.9998			
20	1.81	4.65	0.9997			
25	2.22	4.58	0.9998			
30	2.63	4.76	0.9994			
	iPP + 5wt% CYU201			iPP + 10wt% CYU201		
5	0.56	6.29	0.9998	0.56	5.98	0.9999
10	1.21	4.93	1.0000	1.19	4.73	0.9993
15	1.94	3.86	0.9998	1.84	4.37	0.9999
20	2.33	4.26	0.9998	2.24	4.18	0.9995
25	2.71	4.28	0.9996	2.76	4.03	0.9995
30	3.25	3.81	0.9990	3.17	4.01	0.9992
	iPP + 20wt% CYU201			iPP + 30wt% CYU201		
5	0.51	5.40	0.9988	0.59	4.93	0.9996
10	1.44	4.09	0.9997	1.22	4.90	0.9999
15	1.84	4.39	0.9999	1.57	4.65	0.9995
20	2.33	4.15	0.9999	2.36	4.48	0.9998
25	2.71	4.29	0.9998	2.87	4.32	0.9996
30	3.21	3.95	0.9998	3.14	4.15	0.9993

Table 7.9 Non-isothermal melt-crystallization kinetics for neat and TiO_2-filled based on Avrami analysis over the crystallinity range of 10 to 80% (*continued*)

ϕ (°C min^{-1})	K_A (min^{-1})	n_A	r^2	K_A (min^{-1})	n_A	r^2
	iPP + 5wt% CYU202			iPP + 10wt% CYU202		
5	0.63	7.28	0.9985	0.57	5.53	0.9996
10	1.69	4.90	0.9993	1.08	4.94	0.9993
15	2.39	5.34	0.9979	1.78	4.25	0.9998
20	3.03	4.38	0.9968	2.16	4.37	0.9997
25	3.77	4.22	0.9940	2.74	4.37	0.9998
30	4.15	3.87	0.9895	3.02	4.42	0.9998
	iPP + 20wt% CYU202					
5	0.66	5.40	0.9992			
10	1.36	4.12	0.9986			
15	2.11	3.92	0.9994			
20	2.69	3.91	0.9996			
25	2.95	4.01	0.9982			
30	3.51	3.90	0.9965			
	iPP + 5wt% CYU203			iPP + 10wt% CYU203		
5	0.42	5.60	0.9999	0.43	5.46	0.9998
10	0.86	4.98	0.9992	0.75	5.55	1.0000
15	1.36	4.48	0.9977	1.22	4.85	0.9994
20	1.80	4.34	0.9988	1.64	4.74	0.9996
25	1.98	4.35	0.9993	1.74	5.29	0.9998
30	2.25	4.44	0.9995	2.05	5.09	0.9995
	iPP + 20wt% CYU203			iPP + 30wt% CYU203		
5	0.45	5.54	0.9988	0.46	5.57	0.9986
10	0.79	5.72	0.9996	0.85	6.09	0.9997
15	1.20	5.28	0.9992	1.26	4.79	0.9999
20	1.56	4.93	0.9996	1.97	4.97	0.9996
25	1.91	4.83	0.9998	2.19	5.00	0.9996
30	2.21	4.98	0.9994	2.41	4.76	0.9984

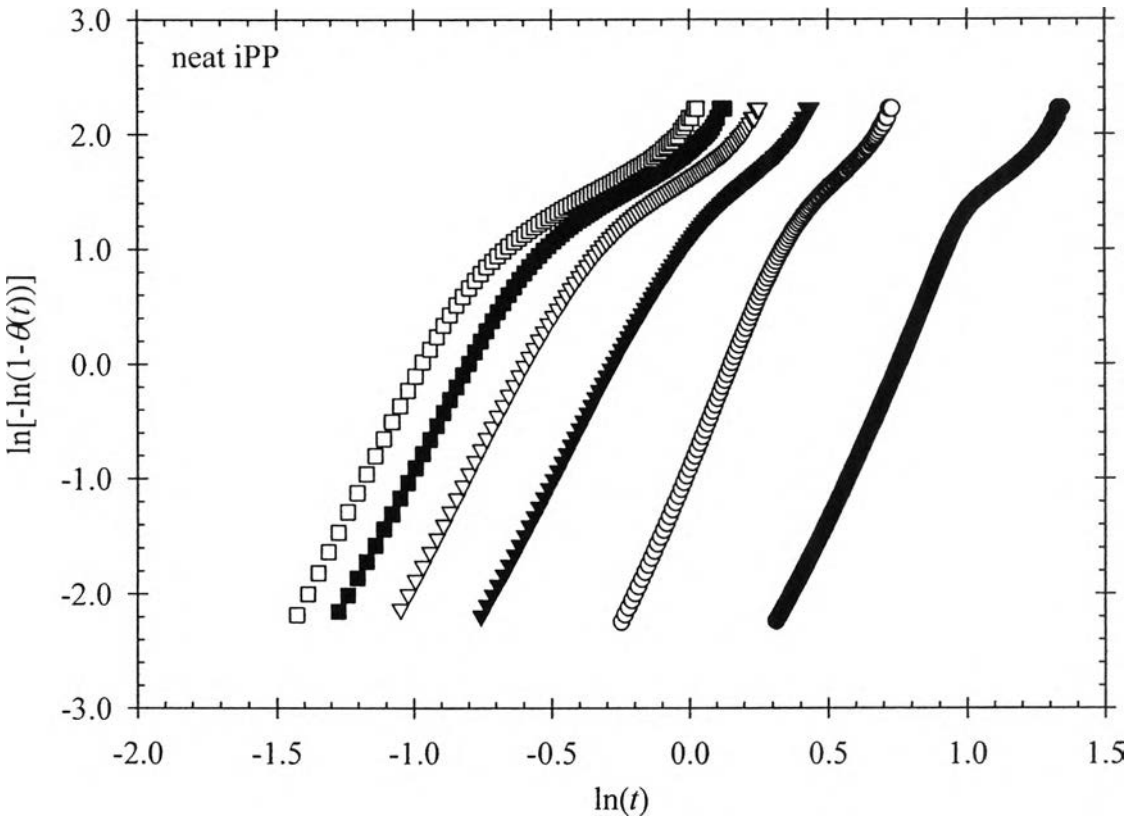

Figure 7.9 Typical Avrami analysis according to the relative crystallinity as a function of time for neat iPP after non-isothermal melt-crystallization at six different cooling rates.

7.5.3 Mechanical Properties

Fig. 7.10 shows the tensile strength at yield for neat iPP and iPP samples filled with various types of TiO_2 nanoparticles. Clearly, the tensile strength at yield generally decreased with increasing TiO_2 content. The observed decrease in the tensile strength at yield is probably due to the poor interfacial adhesion between the TiO_2 nanoparticles and the iPP matrix. Interestingly, the tensile strength at yield for iPP samples filled with stearic acid-coated TiO_2 nanoparticles (CYU203) at any given filler content was comparatively lower than that for iPP samples filled with the other two types of TiO_2 nanoparticles. Previously, Supaphol et al. [6] reported that the tensile strength at yield for sPP samples filled with $CaCO_3$ particles decreased with increasing $CaCO_3$ content and that the surface coating of the particles with

either paraffin or stearic acid reduced the property value of the filled samples. The presence of the TiO_2 nanoparticles within the iPP matrix obviously increased the rigidity (i.e. Young's modulus) of the resulting composites (see Fig. 7.11; especially when the TiO_2 content ≥20wt%). Again, iPP samples filled with stearic acid-coated TiO_2 nanoparticles showed slightly lower Young's modulus than those filled with the other two types of TiO_2 nanoparticles. On the other hand, the elongation at yield of the composites decrease monotonically with the addition of and increasing amount of TiO_2 nanoparticles (see Fig. 7.12). Fig. 7.13 shows the impact resistance for neat iPP and iPP samples filled with various types of TiO_2 nanoparticles. For a given type of TiO_2 nanoparticles, a maximum in the property value was observed at the filler content of about 5 or 10 wt%, depending on the type of surface coating, except for the iPP samples filled with stearic acid-coated TiO_2 particles (CYU203) which exhibited another maximum at the filler content of 30 wt%. For sPP samples filled with $CaCO_3$ particles, a maximum in the impact resistance was also observed at the filler content of about 5 or 10 wt%, depending on the type of surface coating [6]. Figs. 7.14 and 7.15 show the flexural strength and the flexural modulus for neat iPP and iPP samples filled with various types of TiO_2 nanoparticles. For iPP samples filled with neat and SiO_2-coated TiO_2 nanoparticles, the flexural strength was not significantly different from that of the neat iPP, while that of the iPP samples filled with stearic acidcoated TiO_2 nanoparticles was significantly lower. Again, the presence of the TiO_2 nanoparticles within the iPP matrix obviously increased the rigidity (i.e. flexural modulus) of the resulting composites. For any given TiO_2 content, the property value for iPP samples filled with stearic acid-coated TiO_2 particles (CYU203) was lower than those filled with the other two types of TiO_2 particles.

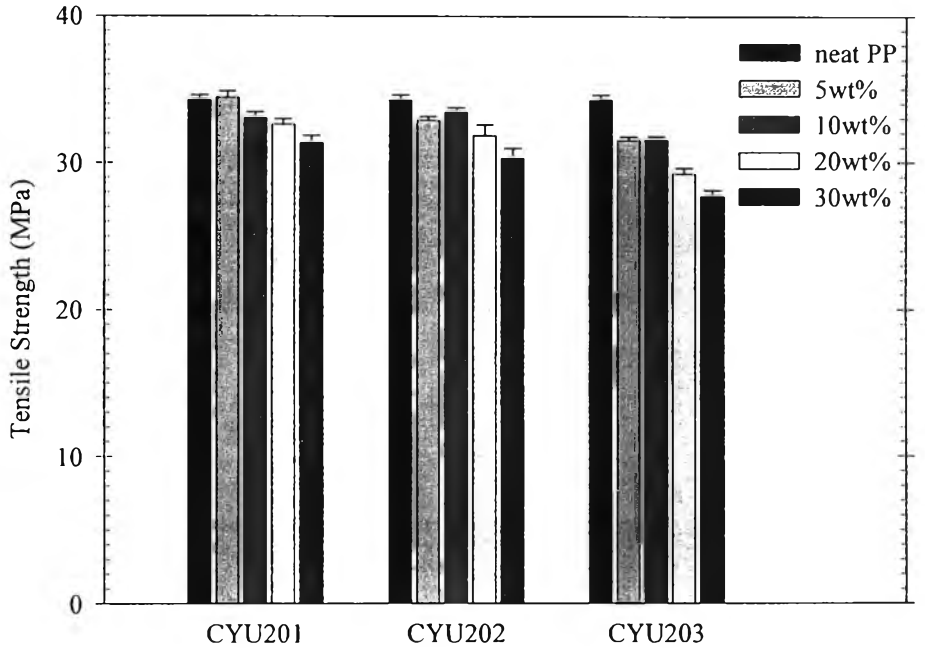

Figure 7.10 Tensile strength at yield for neat and TiO_2-filled iPP

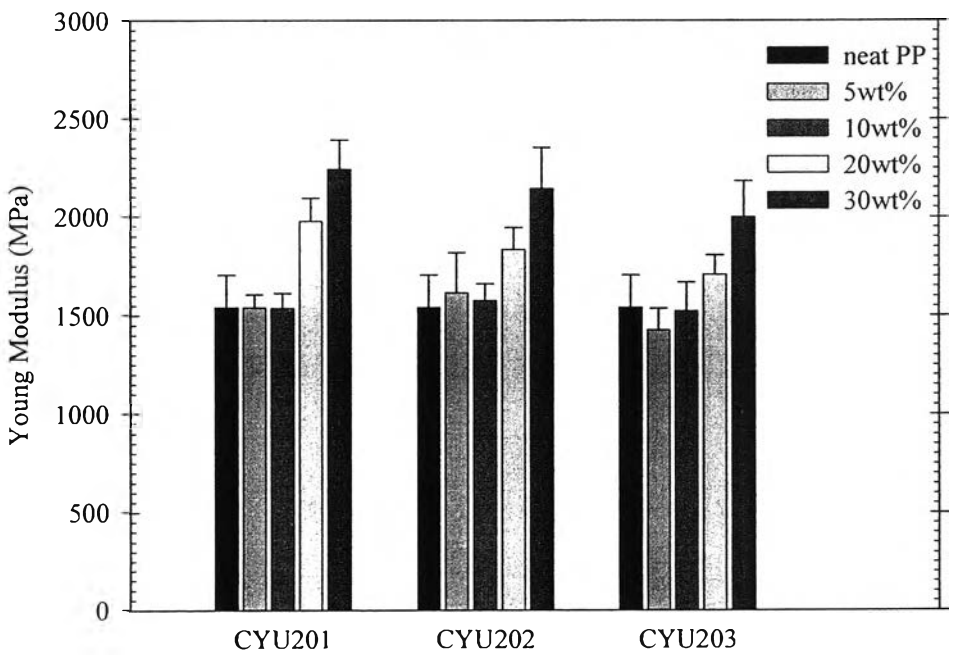

Figure 7.11 Young's modulus for neat and TiO_2-filled iPP.

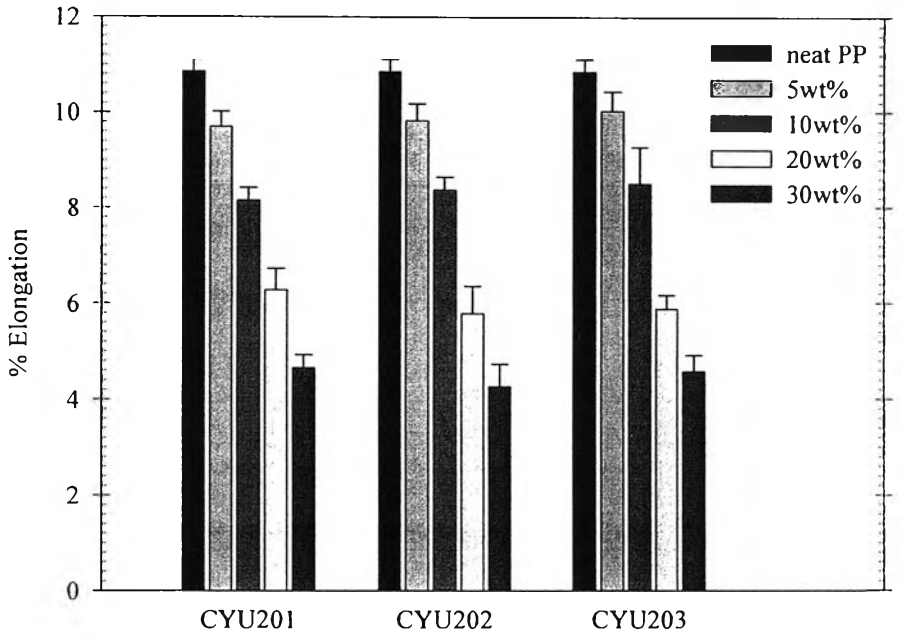

Figure 7.12 Elongation at yield for neat and TiO_2-filled iPP.

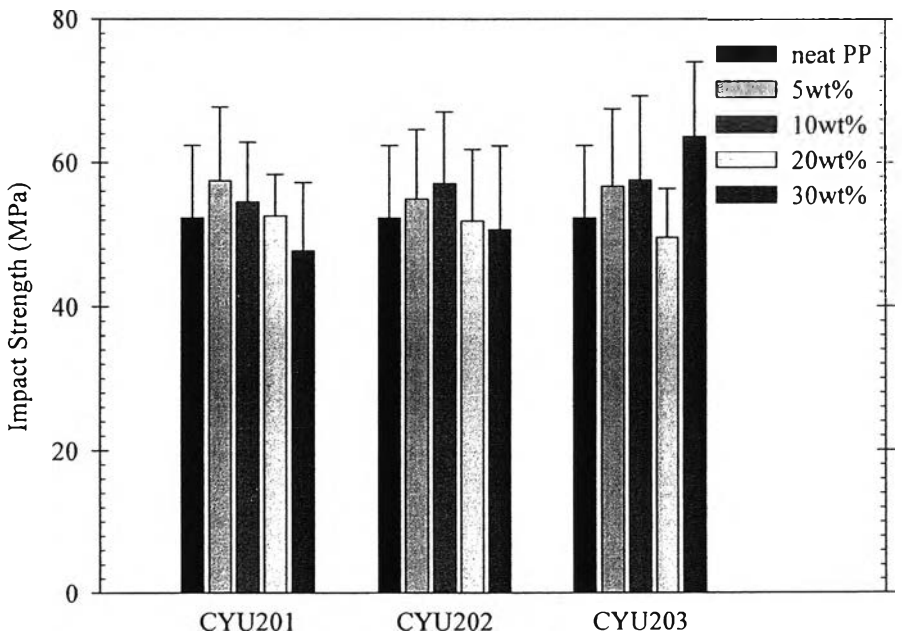

Figure 7.13 Impact resistance for neat and TiO_2-filled iPP.

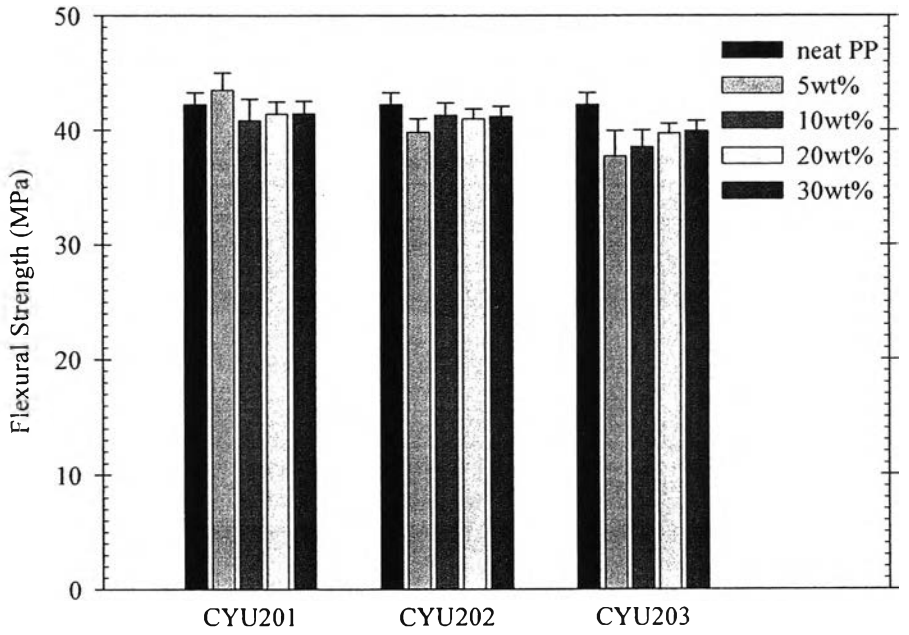

Figure 7.14 Flexural strength for neat and TiO_2-filled iPP.

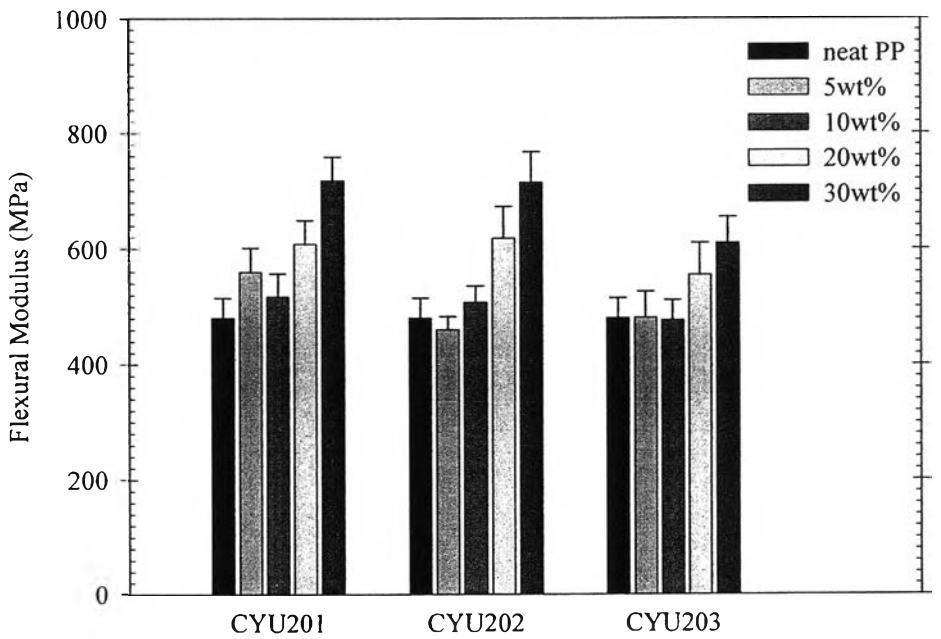

Figure 7.15 Flexural modulus for neat and TiO_2-filled iPP.

7.6 Conclusions

Non-isothermal melt-crystallization and subsequent melting behavior of neat isotactic polypropylene (iPP) and iPP samples filled with titanium(IV)oxide (TiO_2) nanoparticles having different surface characteristics [i.e. neat, silica (SiO_2)-coated, and stearic acid-coated] in various contents ranging from 5 to 30 wt% were investigated using differential scanning calorimetry (DSC). The cooling rates used were ranging from 5 to 30°C min^{-1}. With increasing cooling rate, the crystallization exotherm for all of the samples investigated became larger and shifted towards a lower temperature. The crystallization peak temperature (T_p) for all of the iPP samples filled with neat TiO_2 nanoparticles were slightly greater than those of the neat iPP (by about 1.4–3.6°C) and was not affected by the variation in the filler content (about 2.3–2.6 °C on average). For iPP samples filled with stearic acid-coated TiO_2 nanoparticles, the T_p values were not much different from those of the neat iPP. For iPP samples filled with 5, 20, and 30 wt% SiO_2-coated TiO_2 nanoparticles, marked differences in the T_p values in comparison with those of the neat iPP were observed (about 6.5–7.9 °C on average). Coupled with the crystallization kinetic analysis by the Avrami model, the ability for the various types of TiO_2 nanoparticles to nucleate iPP matrix can be ranked as follows: SiO_2-coated TiO_2 nanoparticles > neat TiO_2 nanoparticles > stearic acid-coated TiO_2 nanoparticles. Lastly, incorporation of the nanoparticles caused the rigidity of the resulting composites to increase (especially when the filler content was greater than or equal to 20 wt%).

7.7 Acknowledgements

This work was supported in part by (1) the Thailand Research Fund (TRF) through the Royal Golden Jubilee Ph.D. Program, (2) the Petroleum and Petrochemical Technology Consortium (through a Thai governmental loan from the Asian Development Bank), and (3) the Petroleum and Petrochemical College, Chulalongkorn University, Thailand.

7.8 References

[1] Y.S. Thio, A.S. Argon, R.E. Cohen, M. Weinberg, Polymer 43 (2002) 3661.

[2] A.L.N. da Silva, M.C.G. Rocha, M.A.R. Moraes, C.A.R. Valente, F.M.B. Coutinho, Polym. Test. 21 (2002) 57.

[3] A. Tabtiang, R. Venables, Eur. Polm. J. 36 (2000) 137.

[4] C.M. Chan, J.S. Wu, J.X. Li, Y.K. Cheung, Polymer 43 (2002) 2981.

[5] J. Gonzalez, C. Albano, M. Ichazo, B. Diaz, Eur. Polym. J. 38 (2002) 2465.

[6] P. Supaphol, W. Harnsiri, J. Junkasem, J. Appl. Polym. Sci. 92 (2004) 201.

[7] S. Miao, Appl. Surf. Sci. 220 (2003) 298.

[8] N.S. Allen, M. Edge, T. Corrales, F. Catalina, Polym. Degrad. Stab. 61 (1998) 139.

[9] T.J. Turton, J.R. White, Polym. Degrad. Stab. 74 (2001) 559.

[10] G.I. Titelman, Y. Gonen, Y. Keider, S. Bron, Polym. Degrad. Stab. 17 (2002) 345.

[11] J. Qian, P. He, K. Nie, J. Appl. Polym. Sci. 91 (2004) 1013.

[12] G.Z. Papageorgiou, D.S. Achilias, D.N. Bikiaris, G.P. Karayannidis, Thermochim. Acta 427 (2005) 117.

[13] S. Jain, H. Goossens, M. Duin, P. Lemstra, Polymer 46 (2005) 8805.

[14] M. Avrami, J. Chem. Phys. 7 (1939) 1103.

[15] M. Avrami, J. Chem. Phys. 8 (1940) 212.

[16] M. Avrami, J. Chem. Phys. 9 (1941) 177.

[17] B. Wunderlich, Macromolecular Physics, vol. 2, Academic Press, New York, 1976, p. 147.

[18] Q.X. Zhang, Z.H. Zhang, H.F. Zhang, Z.S. Mo, J. Polym. Sci.—Polym. Sci. 40 (2002) 1784.

[19] P. Supaphol, P. Thanomkiat, R.A. Phillips, Polym. Test. 23 (2004) 881.

[20] P. Supaphol, P. Charoenphol, J. Junkasem, Macromol. Mater. Eng. 289 (2004) 818.

[21] B. Pukánszky, E. Fekete, Polym. Polym. Compos. 6 (1998) 313.

[22] S. Vleeshouwers, Polymer 38 (1997) 3213.

[23] P. Supaphol, J. Appl. Polym. Sci. 82 (2001) 1083.

[24] K. Trongtorsak, P. Supaphol, S. Tantayanon, Polym. Test. 23 (2004) 533.